AIAA 98-2469
Analysis of Aerospike Plume Induced Base-Heating Environment

T.-S. Wang
NASA-Marshall Space Flight Center
Huntsville, AL

7th AIAA/ASME Joint Thermophysics and Heat Transfer Conference
June 15-18, 1998 / Albuquerque, NM

ANALYSIS OF AEROSPIKE PLUME-INDUCED BASE-HEATING ENVIRONMENT

Ten-See Wang*
NASA Marshall Space Flight Center, Huntsville, AL 35812
email: Ten-see.Wang@msfc.nasa.gov

Abstract

Computational analysis is conducted to study the effect of an aerospike engine plume on X-33 base-heating environment during ascent flight. To properly account for the effect of forebody and aftbody flowfield such as shocks and to allow for potential plume-induced flow-separation, the thermo-flowfield of the entire vehicle at several trajectory points is computed. The computational methodology is based on a three-dimensional, finite-difference, viscous flow, chemically reacting, pressure-based computational fluid dynamics formulation, and a three-dimensional, finite-volume, spectral-line based weighted-sum-of-gray-gases radiation absorption model computational heat transfer formulation. The predicted convective and radiative base-heat fluxes are presented.

Nomenclature

C_1, C_2, C_3, C_μ = turbulence modeling constants, 1.15, 1.9, 0.25, and 0.09
C_p = pressure coefficient
H = total enthalpy
h = static enthalpy
I = radiative intensity
J = Jacobian of coordinate transformation
k = turbulent kinetic energy
N = total number of chemical species
NPR = nozzle to ambient total pressure ratio
P = pressure
Pr = Prandtl number
Q = heat flux, Btu/ft^2-s
q = 1, u, v, w, H, k, ε, or ρ_i
R = recovery factor
S_q = source term for equation q
T^+ = nondimensional temperature
t = time
U = volume-weighted contravariant velocity
u, v, w = mean velocities in three directions
u_τ = wall friction velocity
u^+ = nondimensional velocity, (u/u_τ)
y^+ = nondimensional distance, $(y_p u_\tau \rho/\mu)$
ε = turbulent kinetic energy dissipation rate or wall emissivity
κ = absorption coefficient
μ = effective viscosity, $(\mu_l + \mu_t)$
ξ = computational coordiantes
Π = turbulent kinetic energy production
ρ = density
σ = scattering coefficient
σ_q = turbulence modeling constants
Φ = scattering phase function
φ = energy dissipation function
Ω = direction vector
ω = chemical species production rate

Subscripts
b = black body
c = convective
l = laminar flow
p = off-wall (wall function) point
r = radiative
t = turbulent flow
0 = reference
w = wall surface

---

* Team Leader, Fluid Dynamics Analysis Branch, Member AIAA.

Introduction

In 1996, Lockheed Martin/Skunk Works was selected to build and fly the wedge-shaped "VentureStar" X-33 Advanced Technology Demonstrator for NASA's Reusable Launch Vehicle (RLV) program. The X-33 is a half-scale prototype of a rocket-based single-stage-to-orbit system, which will ultimately be the next-generation RLV. VentureStar will be fueled by liquid hydrogen/liquid oxygen, and features a lifting body configuration coupled with two integrated, cooled linear aerospike rocket engines to propell the vehicle.

It is well known that aerospike engines have the potential advantage of adjusting themselves to perform with maximum efficiency at all altitudes.[1-2] It is less known, however, the heating effect of the hot gases shoot out of the chambers and along the naked, exposed ramp surface on the vehicle components, particularly on the base thermal environment. In order to properly design the thermal protection system of the base components, accurate account of an unified thermo-flowfield around the base region is required.

In this study, as a part of an integrated effort, computational fluid dynamics (CFD) and heat transfer computations were conducted to provide plume-induced base-heating environment for thermal protection system design calculations. Two-dimensional (2D) calculations were performed first and three-dimensional calculations followed. Rationale is given for the methodology and procedure used. Both convective and radiative base-heat fluxes were computed.. The effect of base-bleed is also studied.

Solution Methodology

Computational Grid Generation

Figure 1 shows a full-view of the X-33 surface computational grid. In actual calculations, only 1/2 of the domain is used assuming flow symmetry. A 22-zone, 1,803,614-point baseline grid is generated first, using the software package GRIDGEN.[3] However, the baseline grid topology does not properly capture the complicated flow physics to be addressed and often times causes computational difficulties when the viscous plume flowing across some high aspect-ratio grid regions. A Self-Adaptive Grid codE (SAGEv2)[4] is then used to smooth out the kinks and to efficiently capturing flow physics such as shocks. A typical SAGEv2 smoothed symmetry plane grid is shown in Fig. 2. In addition, the baseline grid had a coarse grid density for the engine ramp region to support one thruster per engine and for a flattened plug-base region which was later replaced by a pillowed-base design. These grid zones were upgraded separately to model 20 thrusters per engine and a pillowed plug-base, as shown in Fig. 3, whereas grid density increased to 2,217,444 points. In general, solution-adapted grid method was used to smooth out the grid distribution in the freestream and far-field plume regions; the patched-grid method was used on zonal interfaces where grid-line discontinuity occurred due to either application of the solution-adaptive grid distribution or a an entire zonal grid replacement; and embedded-grid method was used to locally refine portion or portions of the grid within a grid zone. This grid distribution strategy allows the full-vehicle base-flow physics to be properly captured with a manageable grid size. Figure 2 also shows that the plume is allowed to expand 2.5 times axially the vehicle length, to ensure enough hot plume volume is accounted for base radiative heating calculations.

Thermo-flowfield Computation

Thermo-flowfield solutions about the X33 base-heating environment were carried out with two computational tools: the Finite-Difference Navier-Stokes (FDNS) CFD code[5] for the convective heating and the General Radiation Solution Program (GRASP)[6] for the radiative heating. These tools were developed at MSFC and is continuously being improved by MSFC personnel and its supporting contractors. Systematic and rigorous benchmark studies have been performed on these tools for base flows and heat transfer applications. For example, FDNS has been validated for convective heat transfer inside rocket thrust chambers[7] and coolant channels[8], for base-pressure characteristic curve for a four-engine clustered nozzle configuration[9-10], for Delta Clipper-Experimental (DC-X) base-drag induced by the engine exhaust during cold flow and flight tests[11], and for DC-X convective base-heat flux during landing[12], whereas GRASP has been benchmarked for DC-X radiative base-heat flux during landing[12]. In this study, FDNS and GRASP calculations were conducted sequentially to save computer resources. Later section will show that, this study and the continuous development of these tools, represent an improvement over the conventional design methods in that entire surface heat flux can be mapped instead of discrete body-

point heat flux. In addition, three-dimensional (3D) base-heating can now be simulated. The solution algorithm for the thermo-flowfield computation is summarized in the following.

Convective Heat Transfer

FDNS solves a general curvilinear coordinate, chemically reacting, viscous thermo-flowfield with the formulation of Reynolds-averaged transport equations. A generalized form of these equations is given by

$$\frac{\partial \rho q}{J\partial t} = \frac{\partial\left[-\rho U q + \left(\mu/\sigma_q\right) G\left(\partial q/\partial \xi\right)\right]}{\partial \xi} + \frac{S_q}{J} \qquad (1)$$

A pressure-based predictor-plus-multicorrector solution method is formulated.[13] The basic idea is to perform correction for the pressure and velocity fields by solving for a pressure correction so that the velocity-pressure coupling is enforced, based on the continuity constraint. Second-order central-difference scheme is employed to discretize the diffusion fluxes and source terms of the governing equations. For the convective terms, second-order total-variation-diminishing difference scheme was used in this effort.

An extended k-ε turbulence model[14] is used to describe the turbulence. $\mu_t = \rho C_\mu k^2/\varepsilon$ is the turbulence eddy viscosity. Turbulence modeling constants σ_q and source terms S_q of the transport equations are given in Table 1. These turbulence modeling constants have been used extensively for combustion driven and base flows, while σ_k and σ_ε are taken from the turbulence closure.[14] A 7-species, 9-reaction detailed mechanism[15] was used to describe the finite-rate hydrogen-oxygen afterburning chemical kinetics. The seven species are H_2, O_2, H_2O, O, H, OH, and N_2, whereas H_2O is the only radiating medium.

Table 1 σ_q and S_q of the transport equations

q	σ_q	S_q
1	1.00	0
u	1.00	$-P_x+\nabla[\mu(u_j)_x]-(2/3)(\mu\nabla u_j)_x$
v	1.00	$-P_y+\nabla[\mu(u_j)_y]-(2/3)(\mu\nabla u_j)_y$
w	1.00	$-P_z+\nabla[\mu(u_j)_z]-(2/3)(\mu\nabla u_j)_z$
H	0.95	DP/DT+φ
k	1.00	$\rho(\Pi-\varepsilon)$
ε	1	$\rho(\varepsilon/k)\{[C_1+C_3(\Pi/\varepsilon)]\Pi-C_2\varepsilon\}$
ρ_i	1.00	ω_i, i = 1,...,N

A modified wall function approach is employed to provide near-wall resolution that is less sensitive to the near-wall grid spacing. Consequently, the model has combined the advantages of both the integrated-to-the-wall approach and the conventional law-of-the-wall approach by incorporating a complete velocity profile[16] given by

$$u+ = \ln\left[\left(y^+ + 11\right)^{4.02} / \left(y^{+2} - 7.37y^+ + 83.3\right)^{0.79}\right] + 5.63\tan^{-1}\left(0.12y^+ - 0.441\right) - 3.81 \qquad (2)$$

and a universal temperature profile[17] given by

$$T^+ = u^+ + 12.8(\mathrm{Pr}_l^{0.68} - 1) \qquad (3)$$

The convective heat transfer from a hot boundary layer to a cooler wall follows the modified Newtonian law[12]

$$Q_{cw} = (\rho u_\tau/T^+)[h_w - h_p - R(u_p^2/2)] \qquad (4)$$

where $R = \mathrm{Pr}_l^{1/2}$ if $y^+ \le 11.63$ and $R = \mathrm{Pr}_l^{1/3}$ if $y^+ > 11.63$, whereas $y^+ = 11.63$ is the thickness of the viscous sublayer. Although Pr_l appears both in the heat transfer coefficient and recovery factor terms of Eq. (4), parametric studies performed in Ref. 12 showed that convective heat flux for hydrogen/oxygen plumes exhausting into air is not sensitive to a multicomponent variable Pr_l, hence a constant laminar Prandtl number of air is used.

Radiative Heat Transfer

GRASP analyzes the radiative field by solving the general curvilinear coordinate radiative transfer equation (RTE) with a finite-volume method (FVM) formulation:[18]

$$(\Omega\cdot\nabla)I(r,\Omega) = -(\kappa+\sigma)I(r,\Omega) + \kappa I_b(r) + \frac{\sigma}{4\pi}\int_{\Omega'=4\pi} I(r,\Omega')\Phi(\Omega'\rightarrow\Omega)d\Omega' \qquad (5)$$

where $\Phi(\Omega'\rightarrow\Omega)$ is the scattering phase function from the incoming Ω' direction to the outgoing Ω direction. The term on the left-hand side represents the gradient of the intensity in the direction of Ω. The three terms on the right-hand side represent the

changes in intensity due to absorption and out-scattering, emission, and in-scattering, respectively. The wall boundary is assumed gray whereas emitting and reflecting diffusely, hence the radiative wall boundary condition is given by

$$I(r_w,\Omega^+) = \varepsilon I_b(r_w) + \frac{(1-\varepsilon)}{\pi} \int_{n.\Omega^-<0} I(r_w,\Omega^-)|n.\Omega^-|d\Omega^- \quad (6)$$

with

$$q_{rw} = \int_{n.\Omega^-<0} I(r_w,\Omega^-)|n.\Omega^-|d\Omega^- \quad (7)$$

where Ω^+ and Ω^- denote the leaving and arriving radiative intensity directions, respectively. Notice the angles of the leaving and arriving rays range from 0 to π, whereas the maximum angle of the incoming and outgoing directions in Eq. (5) is 4π. The 20-band spectral-line weighted sum of gray gases model[6] is used to calculate the total emissivity and absorptivity of the radiating medium. Following the ray-dependency test performed in Ref. 12, the FVM 6x4 option is deemed as adequate and used in this effort. The FVM 6x4 option has six control angles in the polar direction and four in the azimuthal direction.

Boundary and Initial Conditions

The outer boundary of the computational domain comprises of fixed total condition free-stream flow boundaries, one symmetry plane, and the remaining flow exit plane. No-slip walls are specified for the body surfaces. A fixed (ambient) static pressure is imposed on the exit plane and on a point far away from the action area, in order to obtain an unique solution for the desired altitude. The fixed inlet boundary condition is applied to the thruster exit plane where the flow property is mapped from a separate 3D thruster CFD solution. That separate calculation was started from the subsonic chamber, to ensure the correct nozzle exhaust flow property, including internal boundary-layer growth, nozzle shock strength and location, and turbulence level. The subsonic chamber inlet-flow property was obtained from a thermo-equilibrium analysis[19] using engine conditions. This procedure of performing a separate thrust chamber calculation is crucial to the final solution[11] since the propulsive nozzle flow is the source of the base-flow physics. The fixed inlet boundary condition is also applied to the base-bleed region on the plug-base.

For convective heat transfer calculations, ambient temperature is prescribed as the forebody surface temperature, whereas 540 R is specified for all base surfaces per base-heating design convection. For radiation calculations, the surface emissivity of the entire vehicle is assumed to be 0.7. The engine ramp is actively cooled and the surface temperature distribution is prescribed from a separate conjugate heat transfer calculation involving solid walls and coolant channel flows. It is found in this work (2D, M = 0.60) that cowl base irradiation is more than ten times higher if adiabatic condition is imposed on the ramp surface.

Results and Discussion

2D Base-Heating Environment

Six 2D X33 aerospike engine base flowfields are computed for Mach numbers 0.00, 0.60, 0.98, 1.72, 2.81, and 4.07. The computational domain covers the aftbody, cowl base, thruster, engine ramp, plug base and plume expansion region about 9 times the plug-base half-width. These cases essentially simulate a 2D cut of the 3D domain at the symmetry plane, without a realistic influence from the forebody flow. Nevertheless, these 2D computations provide valuable insight to the approximate base-flow physics at a very fast turnaround time. For example, the effect of engine running at reduced power level can be had quickly. Figure 4 shows a comparison of the predicted plug-base (flattened) convective heat fluxes. It can be seen that the plug-base convective heat fluxes decrease with increasing altitudes (freestream Mach numbers). More importantly, at a fixed altitude, the difference in convective heat fluxes between using frozen chemistry and finite-rate chemistry becomes negligible as freestream Mach number exceeds 0.98 - an indication of diminishing plume afterburning due to air dilution. This result leads to the frozen chemistry assumption in the 3D computation for supersonic freestreams. It is also found in 2D studies that local time-stepping can only be utilized in the initial stage to facilitate the solution development. Constant time steps must be followed to ensure synchronized time-marching to avoid false base flow-physics caused by biased local-flow residence time distribution.

3D Base-Heating Environment

Freestream Mach numbers of 0.60, 1.72, 2.81, and 4.07 are chosen for the 3D full-vehicle base environment computations. The 3D base flow physics such as the plume jumping on the cowl-base, plume spillage on the side-ramp, reverse jet impingement on the plug-base, lateral wall-jet impingement on the inboard- and outboard-bases are highly three-dimensional and heavily depend on the forebody and aftbody flowfields. Of particular interests are the inboard and outboard base-heating due to the lateral wall-jet impingement, and whether there is plume induced flow separation (PIFS) occurring at M = 4.07 to affect the topside panel opening for pressure balance purpose.

The accuracy of forebody and aftbody flowfields is assessed by comparing surface pressures with limited cold-flow test data. The 7.75% scaled model has a different ramp configuration and was running at lower NPR ratios. For those reasons, only the forebody and aftbody surface pressures are compared. Figure 5 shows such a comparison for M = 1.72 at the symmetry plane with those of the cold-flow test at M =1.60 and M = 1.80. The comparison is very good since the signal from the propulsive plume does not transmit forward due to the supersonic freestream and thin boundary layer. For M = 0.60 case, as shown in Fig. 6, the comparison is in general reasonable except for the aftbody region, where the cold flow model has a lower surface pressure than that of the flight simulation. This discrepancy is expected since in subsonic flow environment, the aftbody surface pressure is affected by variations in ramp configuration, jet molecular weight, and NPR. In additon, the cold jets tend to produce higher drag[20] - a higher entrainment that tends to accelerate the flow over the aftbody resulting in a decrease in the aftbody surface pressure. These comparisons indicate that the forebody and aftbody flow is adequately simulated for base flow development. Under those circumstances, base-bleed does not influence forebody and aftbody surface pressures.

Several computed full-vehicle surface heat-flux contours are presented in the following figures, with emphasis on the vehicle-base side. Different scales are used for different regions such that the flow physics can be revealed. Figure 7 shows the convective heat-flux contours without base-bleed for M = 0.60. The heat fluxes are at its highest on the engine ramp surface since the ramp is part of the exposed nozzle. An unique heat flux pattern is formed on the plug-base due to the interaction of the reverse jet and the lateral wall-jet with the pillowed-base. In general, the base heat fluxes decrease with increasing altitudes, whereas the plug-base lateral wall jet impingement with the inboard and outboard surface increases with increasing altitudes. Figure 8 shows the convective heat flux contours with base-bleed at M = 4.07. The effect of lateral wall jet impingement on the outboard base can be clearly seen. The convective heating to the base-bleed region itself can not be computed with the current model, but the heating on the rest of the plug-base is lowered due to base-bleed.

Figures 9 and 10 show the radiative base heat-flux contours for M = 0.60. Generally, the characteristics of the computed radiative heat-flux contours look dissimilar to those of the convection (Fig. 7 and 8). The convective heating is transported through direct contact of the surface with the propulsive flow, whereas the radiative heating is transported through space from the hot plume to the surface and the view factor. For example, in the M = 0.60 case, the inner side of the vertical fin showed effect of radiative heating but not convective heating (Fig. 7 and 8). In addition, the top and bottom parts of the inboard and outboard bases show signs of radiative heating but not in the middle section, indicating the view from the middle part is blocked by the nozzle plug in the near field. It can also be seen that the plug-base radiative heating is lowered with the protection of the base-bleed. Although the surface irradiation is suppressed in Fig. 9-10 due to the surface temperature treatment, the effect is always included with GRASP. This is another improvement over the conventional plume radiation calculation in which the surface radiation is not included.

In this study, PIFS is not observed for all four trajectory points.

Conclusion

A computational methodology is developed to study the 3D X-33 aerospike engine plume induced base-heating environment. Three grid distribution methods are utilized to minimize the grid requirement of a full-vehicle thermo-flowfield computation: solution-adaptive, patched, and embedded grid schemes. The 3D base-flow physics such as plume jumping, plume spillage, plug-base reverse jet formation, and plug-base lateral wall jet impingement with the inboard- and outboard-base surfaces are captured. The effect of base-bleed is studied. The methodology and procedure developed in this study represent an improvement in the base-heating design area over the conventional method in several aspects.

Acknowledgment

This work was performed under the cooperative agreement between Lockheed martin Skunk Works and NASA Marshall Space Flight Center for the Phase II Reusable Launch Vehicle/X-33 Technology Development Program. Robert Williams generated the baseline 3D grid and Joni Cornellison generated the refined 3D engine ramp and pillowed plug-base grids. Mark D'Agostino provided forebody surface pressure wind tunnel test data. Mark Seaford coordinated the MSFC RLV/X-33 base-heating effort. The patched- and embedded-grid formulations were developed by Engineering Sciences, Inc. under a separate "Injector Design Tool Improvements" contract.

References

[1] Huang, D.H., "Aerospike Engine Technology Demonstration for Space Propulsion," AIAA Paper 74-1080, Oct. 1974.

[2] Lamont, E.A., "The Aerospike Engine System for the Space Tug - A Status Report," AIAA Paper 73-1245.

[3] Steinbrenner, J.P., Chawner, J.R., and Pouts, C., "Multiple Block Grid Generation in the interactive Environment," AIAA Paper 90-1602, June 1990.

[4] Davies, C.B., and Venkatapathy, E., "The Multidimensional Self-Adaptive Grid Code, SAGEv2," NASA TM 110350, April 1995.

[5] Chen, Y.-S., "FDNS - A General Purpose CFD Code, Version 4.0," Engineering Sciences, Inc., ESI-TR-97-01, Huntsville, AL, May 1997.

[6] Liu, J., Shang, H.-M., Chen, Y.-S., and Wang, T.-S., "GRASP: A general Radiation Simulation Program," AIAA Paper 97-2559, June, 1997.

[7] Wang, T.-S., and Luong, V., "Hot-Gas-Side and Coolant-Side Heat Transfer in Liquid Rocket Engine Combustors," *Journal of Thermophysics and Heat Transfer*, Vol. 8, No. 3, 1994, pp. 524-530.

[8] Wang, T.-S., and Chyu, M.K., "Heat Convection in a 180-Deg Turning Duct with Different Turn Configurations," *Journal of Thermophysics and Heat Transfer*, Vol. 8, No. 3, 1994, pp. 596-601.

[9] Wang, T.-S., "Numerical Analysis of Base Flowfield for a Four-Engine Clustered Nozzle Configuration," *Journal of Propulsion and Power*, Vol. 11, No. 5, 1995, pp. 1076-1078.

[10] Wang, T.-S., "Grid-Resolved Analysis of Base Flowfield for Four-Engine Clustered Nozzle Configuration," *Journal of Spacecraft and Rockets*, Vol. 33, No. 1, 1996, pp. 22-29.

[11] Wang, T.-S., and Cornelison, J., "Analysis of Flowfields over Four-Engine DC-X Rockets," *Journal of Spacecraft and Rockets*, Vol. 34, No. 5, 1997, pp. 620-627.

[12] Wang, T.-S., "Delta Clipper-Experimental In-Ground Effect on Base-Heating Environment," *Journal of Thermophysics and Heat Transfer*, Vol. 12, No. 2, 1998.

[13] Wang, T.-S., and Chen, Y.-S., "Unified Navier-Stokes Flowfield and Performance Analysis of Liquid Rocket Engines," *Journal of Propulsion and Power*, Vol. 9, No. 5, 1993, pp. 678-685.

[14] Chen, Y.-S., and Kim, S. W., "Computation of Turbulent Flows Using an Extended k-ε Turbulence Closure Model," NASA CR-179204, Oct. 1987.

[15] Wang, T.-S., McConnaughey, P., Chen, Y.-S., and Warsi, S., "Computational Pollutant Environment Assessment from Propulsion System Testing," *Journal of Spacecraft and Rockets*, Vol. 33, No. 3, 1996, pp. 386-392.

[16] Liakopolous, A., "Explicit Representations of the Complete Velocity Profile in a Turbulent Boundary Layer," *AIAA Journal*, Vol. 22, No. 6, 1984, pp. 844-846.

[17] White, F.M., *Viscous Fluid Flow*, McGraw-Hill, New York, 1974.

[18] Liu, J., Shang, H.-M., Chen, Y.-S., and Wang, T.-S., "Prediction of Radiative Transfer in General Body-Fitted Coordinates," *Numerical Heat* Transfer, Part B, Vol. 31, 1997, pp. 423-439.

[19] Svehla, R.A., and McBride, B.J., "FORTRAN IV Computer Program for Calculation of Thermodynamic and Transport Properties of Complex Chemical Systems," NASA TN D-7056, Jan. 1973.

[20] Peters, W.L., "A Comparison of Jet Temperature Effects on Afterbody Drag with Those from Jet Molecular Weight and Nozzle Area Ratio Variations," AIAA Paper 80-1161.

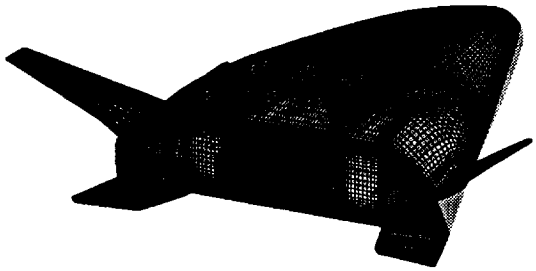

Fig. 1 Layout of the X-33 surface computational grid.

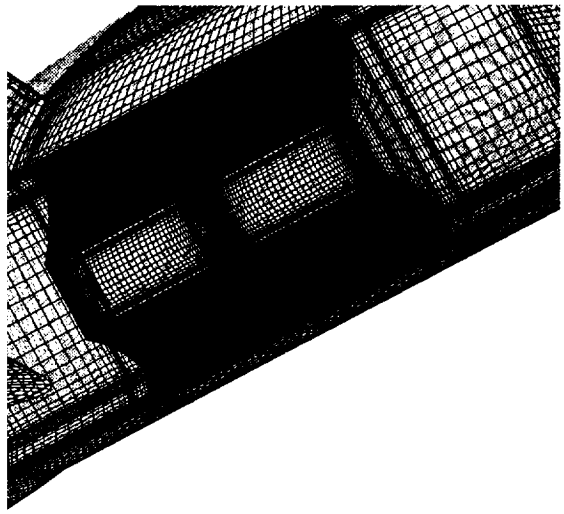

Fig. 3 Close-up look grid of the thruster, engine ramp and pillowed plug-base grid.

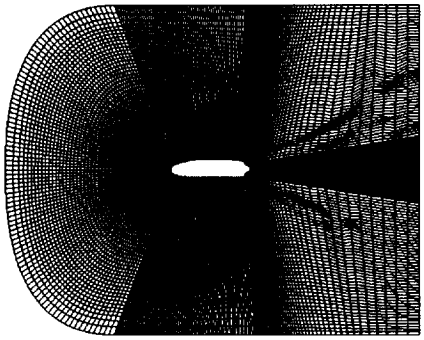

Fig. 2 Grid distribution of a typical symmetry plane grid.

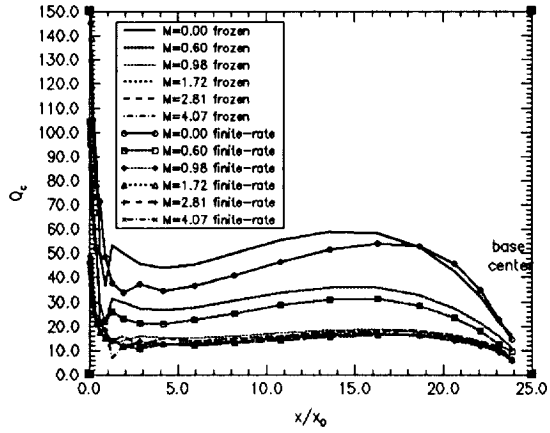

Fig. 4 Comparison of the 2D computation predicted plug-base convective heat fluxes.

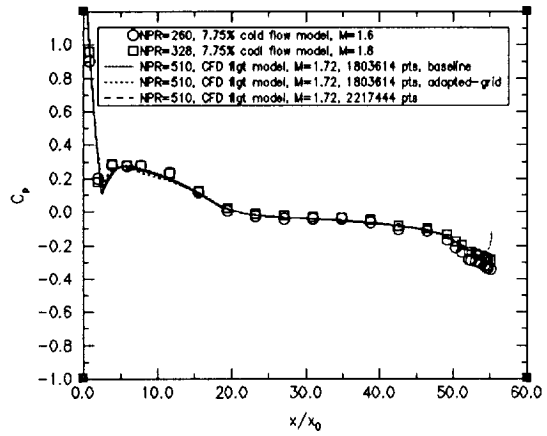

Fig. 5 Comparison of the X33 forebody and aftbody surface pressure coefficients.

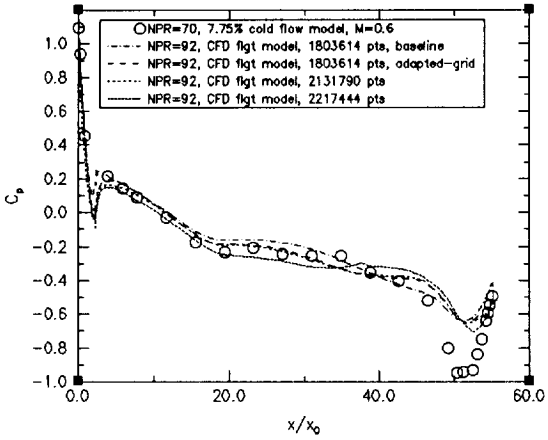

Fig. 6 Comparison of the X33 forebody and aftbody surface pressure coefficients.

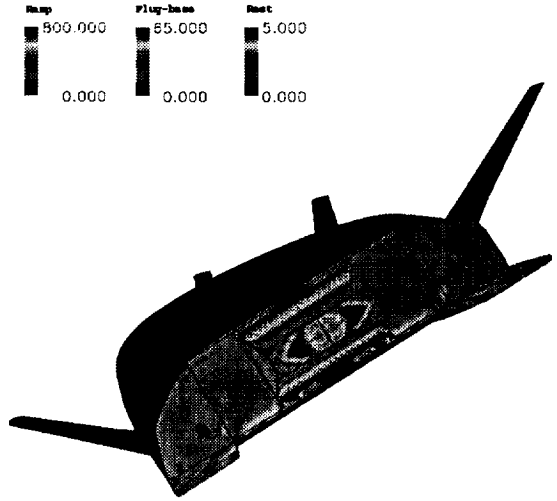

Fig. 7 Convective heat fluxes without base-bleed for M = 0.60.

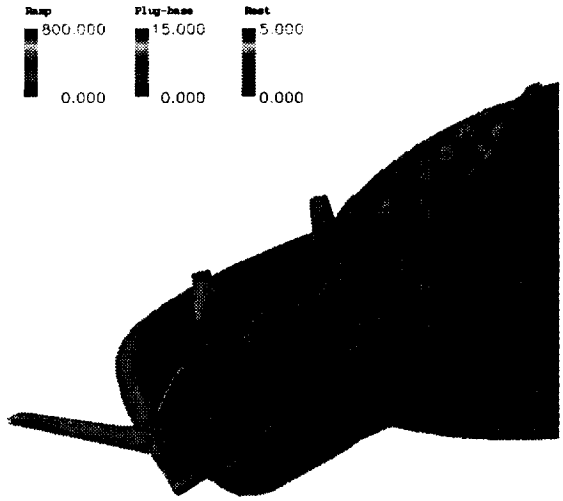

Fig. 8 Convective heat fluxes with base-bleed for M =4.07 with exhaust plume.

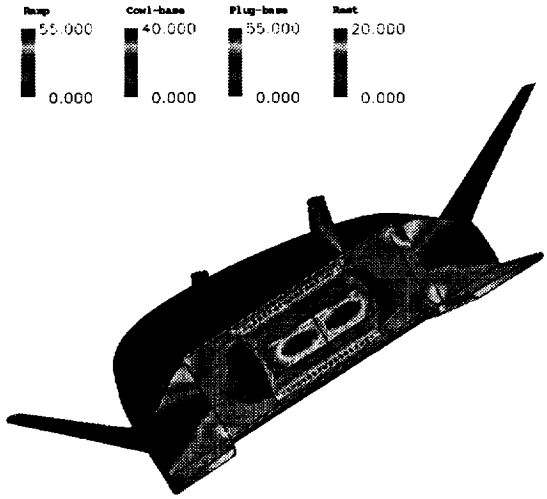

Fig. 9 Radiative heat fluxes without base-bleed for M =0.60.

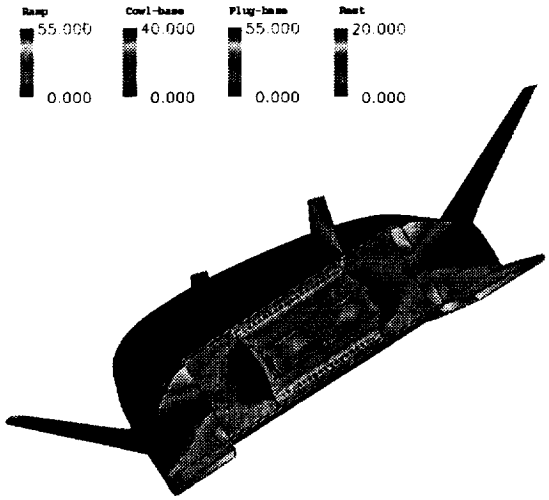

Fig. 10 Radiative heat fluxes with base-bleed for M = 0.60.